Design principles for radiation-resistant solid solutions

Thomas Schuler,* Dallas R. Trinkle, Pascal Bellon, and Robert Averback
Department of Materials Science and Engineering, University of Illinois, Urbana-Champaign, Illinois 61801, USA
(Received 15 December 2016; revised manuscript received 28 February 2017; published 10 May 2017)

We develop a multiscale approach to quantify the increase in the recombined fraction of point defects under irradiation resulting from dilute solute additions to a solid solution. This methodology provides design principles for radiation-resistant materials. Using an existing database of solute diffusivities, we identify Sb as one of the most efficient solutes for this purpose in a Cu matrix. We perform density-functional-theory calculations to obtain binding and migration energies of Sb atoms, vacancies, and self-interstitial atoms in various configurations. The computed data informs the self-consistent mean-field formalism to calculate transport coefficients, allowing us to make quantitative predictions of the recombined fraction of point defects as a function of temperature and irradiation rate using homogeneous rate equations. We identify two different mechanisms according to which solutes lead to an increase in the recombined fraction of point defects; at low temperature, solutes slow down vacancies (kinetic effect), while at high temperature, solutes stabilize vacancies in the solid solution (thermodynamic effect). Extension to other metallic matrices and solutes are discussed.

DOI: 10.1103/PhysRevB.95.174102

I. INTRODUCTION

The development of future nuclear reactors requires materials able to withstand irradiation damage levels that are higher than in current nuclear reactors [1,2]. Reaching this high radiation resistance raises new challenges since point defects created under irradiation lead to a wide range of potentially harmful effects [3–5]: radiation-induced segregation [6–8], radiation-induced precipitation [9–11], dislocation climb and irradiation creep [12–14], formation of point-defect clusters, which lead to swelling [15–17] and embrittlement [18,19]. Since many of these phenomena result from point-defect diffusion to sinks, there are two main approaches to mitigate these effects, either by reducing the irradiation-induced point-defect supersaturation, or by reducing the mobility of the point defects. As we discuss below, these approaches can be implemented by controlling the microstructure and/or optimizing the composition of the materials of interest.

Point defects created under irradiation are annihilated either by athermal recombination between a vacancy and a self-interstitial atom or by elimination at sinks like free surfaces, dislocations, grain boundaries, or interfaces. As a consequence, when the goal is to reduce the point-defect supersaturation, a common approach has been to devise microstructures with a very high density of sinks and/or efficient point-defect sinks, such as nanolaminates and nano-oxide-dispersion strengthened alloys [20–23]. The long-term stability of these materials is however problematic as a large number of interfaces often undergo coarsening. Another possible solution is to rely on irradiation-induced self-organization to stabilize nanoprecipitates under steady-state irradiation, thus providing a high density of stable precipitate-matrix interfaces [24–27]. Increasing point-defect elimination at sinks, however, can lead to long-range solute redistribution due to the kinetic coupling between point-defect fluxes and solute fluxes. The long-term behavior of both sinks and bulk material must therefore be investigated thoroughly.

The alternative strategy—pursued here—is to reduce the mobility of point defects, so as to increase their recombination rate. This approach has the advantage of relying on a local phenomenon and does not lead to chemical redistribution over large distances. This approach has been considered in the past, in particular to reduce or suppress radiation-induced segregation, swelling and creep [28–34]. Specifically, solute additions were used to slow down vacancies and/or self-interstitials, leading to higher total point-defect concentrations in the system, and consequently increasing the recombination rate. In some cases, solute additions were effective in suppressing radiation-induced segregation at grain boundaries but the effect seemed to fade away after a radiation damage level of a few displacements per atom [32,34]. From these previous studies, however, there are conflicting arguments about how to select relevant solutes: some of them recommend undersized solutes to trap self-interstitials [29], while others recommend oversized solutes to trap vacancies [32,34], or oversized solutes to trap self-interstitials [33]. For instance, Mansur *et al.* state that vacancies and self-interstitial atoms have the same effect on recombination when the difference in solute-point-defect binding energies is equal to the difference in point-defect bulk migration energies [30,31]. They used a rate theory model which includes trapped point defects to calculate the evolution of point-defect concentrations under irradiation and assess the effect of trapping on swelling and creep. Their model, however, assumes that traps are immobile whereas substitutional solutes with a high binding energy to a vacancy are usually fast diffusers. Therefore increasing the recombined fraction of point defects requires solutes, which (1) have an attractive binding energy to point defects, (2) reduce defect mobility with respect to a pure matrix, and (3) remain in solution (i.e., resist radiation-induced segregation).

In the past, it was not possible to assess quantitatively these three required properties for a broad range of solute elements, and assumptions had to be made, particularly on the transport contribution. Electronic structure calculations show that there are no simple and systematic correlations between atomic size, misfit strain, excess valence, solubility limits and the quantities of interest, i.e., solute-point-defect binding and

*Corresponding author: tschul@illinois.edu

diffusivity [35,36]. For instance, the migration energies of a vacancy around a solute relates to the bonding characteristics of d electrons of solute atoms [35]; the overall solute diffusivity being a complicated function of all these migration energies [37–39], it cannot be predicted from solute properties in a bulk material. Fortunately, recent advances in atomistic and continuum modeling of transport of solutes and point defects now make it possible to systematically screen and select the most promising solutes for increasing point-defect recombination. Specifically, large-scale first-principles calculations provide accurate binding and migration energies for a wide range of solutes, thus addressing the first property identified above for solutes to increase point-defect recombination. This atomistic information can be used to inform the self-consistent mean-field (SCMF) theory to calculate transport coefficients. Furthermore, recent developments of the SCMF method [39] have made it possible to calculate the transport coefficients for defect-solute pairs, thus enabling the identification of solutes meeting the second and the third requirements to increase point-defect recombination. By combining these techniques, we show here that there exist solutes in a Cu matrix that can trap point defects effectively and thus enhance recombination, while resisting radiation-induced segregation. This study thus provides general design principles for radiation-resistant solid solutions.

The paper is organized as follows. Section II presents the multiscale methodology developed in this study. Homogeneous rate theory equations provide analytical relations between the fraction of recombined point defects and solute properties (Sec. II A). Then we introduce the framework for computing transport coefficients in dilute solid solutions using the self-consistent mean-field method (SCMF) (Sec. II B). In Sec. III, we apply this methodology to a Cu dilute solid solution, which is chosen as a model face-centered cubic material. Using available diffusivity data, we identify Sb as the most efficient solute to increase the fraction of recombined point defects in Cu (Sec. III A). We combine density functional theory (Sec. III B) and SCMF (Sec. III C) to compute all the thermodynamic and kinetic parameters required to apply our rate theory model to Cu(Sb) alloys. We then use rate equations to calculate the efficiency of Sb addition to promote point-defect recombination as a function of irradiation temperature and displacement rate (Sec. III D) and compute the solute point-defect flux coupling properties (Sec. III E). Finally, Sec. IV discusses the effect of point-defect clusters, the experimental validation and the applicability of our formalism to other systems.

II. MULTISCALE METHODOLOGY

A. Rate theory model

The kinetic evolution of point defects in pure systems is commonly modeled using rate equations [5]. Following the work of Mansur [30], we consider here the extension of this approach to dilute solid solutions, by defining total point-defect concentrations per unit volume $[\bar{d}]$ and average point-defect diffusivities $\bar{D}_d$, where d is either a vacancy $d = V$ or a self-interstitial atom $d = I$. The total d concentration includes both isolated point defects and solute-point-defect clusters, and $\bar{D}_d$ corresponds to a thermodynamic average of the diffusivity of d as an isolated defect and as part of a solute-point-defect cluster. In contrast, $[d]$ and D_d respectively define the concentration and diffusivity of isolated point defects. Assuming the solid solution to be dilute such that we can safely neglect clustering reactions (both solute and point-defect clustering), the homogeneous rate equation for defect d is

$$\frac{d}{dt}[\bar{d}] = \frac{\phi}{\Omega} - k_d^2 \bar{D}_d([\bar{d}] - [\bar{d}]^{\mathrm{eq}}) - 4\pi r_c(\bar{D}_V + \bar{D}_I)[\bar{V}][\bar{I}], \tag{1}$$

where ϕ is the irradiation flux, Ω is the atomic volume; k_d^2 is the total sink strength for defect d, $[\bar{d}]^{\mathrm{eq}}$ is the total equilibrium concentration of defect d per unit volume, and r_c is the recombination radius, i.e., the distance below which V and I spontaneously recombine. We assume r_c to be independent of solute concentration or temperature. Note that because defect diffusion coefficients are averaged quantities, the recombination term in Eq. (1) contains several contributions, four in the dilute alloy limit: recombination between V and I, V and IX, VX and I, VX and IX, where VX (respectively, IX) denotes a cluster formed by one vacancy (self-interstitial) and one solute. Considering Eq. (1) for $d = I$ at steady state, one can express $[\bar{I}]$ as a function of $[\bar{V}]$, which is then inserted into Eq. (1) for $d = V$, and provides a second-order polynomial equation for $[\bar{V}]$. Point defects created under irradiation either recombine or eliminate at sinks and the fraction of recombined point defects F_R determines which of these two mechanisms dominates for given irradiation conditions. This fraction F_R is defined as

$$F_R = \frac{1}{1 + \frac{k_I^2 \bar{D}_I([\bar{I}]-[\bar{I}]^{\mathrm{eq}})}{4\pi r_c(\bar{D}_V+\bar{D}_I)[\bar{V}][\bar{I}]}} \simeq \frac{1}{1 + \frac{k^2}{4\pi r_c[\bar{V}]}}, \tag{2}$$

which highlights the fact that a high total vacancy concentration (or a low sink density) is needed to obtain a recombined fraction close to unity. The approximate equality in Eq. (2) assumes $[\bar{I}]^{\mathrm{eq}} \ll [\bar{I}]$, $\bar{D}_V \ll \bar{D}_I$, and unbiased sinks ($k_V^2 = k_I^2 = k^2$). The total vacancy concentration is thus a crucial parameter, and is analytically obtained from Eq. (1). If we assume further that $[\bar{V}]^{\mathrm{eq}} \ll [\bar{V}]$, $[\bar{V}]$ is expressed as

$$[\bar{V}] \simeq \frac{k^2}{8\pi r_c}\left(-1 + \sqrt{1 + \frac{16\pi r_c \phi}{\Omega k^4 \bar{D}_V}}\right). \tag{3}$$

This equation shows that when microstructural parameters (k^2) and irradiation conditions (ϕ) are prescribed, the only way to increase $[\bar{V}]$ is to decrease $\bar{D}_V$, which is reasonable: if vacancies move more slowly, they will spend more time in the material before being eliminated at sinks, thus increasing the probability that they recombine with a self-interstitial atom. At high temperature, $[\bar{V}]^{\mathrm{eq}}$ may not be negligible anymore, and in that regime $[\bar{V}] \simeq [\bar{V}]^{\mathrm{eq}}$. Thus the solutes must decrease the average vacancy diffusivity and/or increase the total equilibrium vacancy concentration, depending on temperature. One of the objectives of this study is to provide a framework to quantify the effect of solute additions on $[\bar{V}]^{\mathrm{eq}}$ and $\bar{D}_V$.

These two quantities can be re-expressed in terms of solute-point-defect properties. Furthermore, we assume that local equilibrium is obeyed everywhere in the system, meaning that in any given volume of the system, the relative probability of isolated species (defect or solute) and pair clusters follows a Boltzmann equilibrium distribution constrained by the local nominal concentration of defects and solutes [40–42]. In this framework, the dX cluster concentration is $[dX] = \Omega[d][X]z_{dX}$ and the total defect concentration is [43,44]

$$[\bar{d}] = z_d[d] + \Omega[d][X]z_{dX}, \tag{4}$$

where $[X]$ is the concentration of isolated solutes; z_d is the geometric multiplicity per site of defect d ($z_V = 1$ and $z_I = 3$, see Appendix B); z_{dX} is the dX pair cluster partition function, which contains the binding energy $[E_b(dX_\rho)]$ and configurational entropy (related to the geometrical multiplicity g_ρ) for all microscopic configurations ρ considered as a dX pair (ensemble ρ_{dX}). The binding energy is the energy difference between d and X being infinitely separated, and d and X being in configuration ρ [see Eq. (C1)]:

$$z_{dX} = \sum_{\rho\in\rho_{dX}} g_\rho \exp\left(\frac{E_b(dX_\rho)}{k_B T}\right). \tag{5}$$

The total equilibrium defect concentration appearing in Eq. (1) can be significantly affected by solute additions, which can reduce the driving force for point-defect elimination at sinks [44]. It is useful to re-express the total equilibrium defect concentration as a function of the equilibrium defect concentration in the absence of solute

$$[\bar{d}]^{\text{eq}} = \left(z_d + \frac{\Omega[\bar{X}]z_{dX}}{1 + \Omega(z_{VX}[V]^{\text{eq}} + z_{IX}[I]^{\text{eq}})}\right)[d]^{\text{eq}}, \tag{6}$$

where $[d]^{\text{eq}} = \exp(-E_f(d)/k_B T)$. Equation (6) shows that increasing the nominal equilibrium vacancy concentration requires $\Omega[\bar{X}]z_{VX} > 1$, which means that a high solute concentration and/or a high vacancy-solute binding energy is required. If the solute concentration is too high (typically $\Omega[X] > 1$ at.%), however, the dilute solid solution approximation breaks down.

We now express $\bar{D}_d$ as a thermodynamic average of cluster transport coefficients, which generalizes the expression introduced by Flynn for the diffusion of defects in the presence of solute-defect clusters [45]:

$$\begin{aligned}\bar{D}_d &= \frac{z_d[d]D_d + \Omega[d][X]z_{dX}L_{dd}(dX)}{z_d[d] + \Omega[d][X]z_{dX}} \\ &= D_d\left(\frac{1 + \Omega[X]z_{dX}L_{dd}(dX)/z_d D_d}{1 + \Omega[X]z_{dX}/z_d}\right).\end{aligned} \tag{7}$$

The kinetic properties of defect d are fully contained in the Onsager or transport coefficient L_{dd} which relates the defect flux to the defect driving force [46]. However, we use the dX pair cluster transport coefficient $L_{dd}(dX)$ to isolate the effect of solute X on the average diffusivity of defect d [39]. This $L_{dd}(dX)$ coefficient contains two contributions: the mobility of a dX cluster that would never dissociate; and the mobility of the defect around the solute which includes association and dissociation jumps (see Sec. II B for details). In previous studies, $L_{dd}(dX)$ was assumed to be 0 (immobile solute trap [30,31]) or equal to the dX cluster mobility only (bound dX pairs migrate as indivisible clusters [45,47,48]). From Eq. (7), solutes will slow down V with respect to the pure metal if $L_{VV}(VX) < D_V$, and $L_{VV}(VX)$ should be as low as possible. However, this criterion alone does not guarantee that a given solute slows down vacancies in a non-negligible way. Immobile solutes ($L_{VV}(VX) = 0$) should in principle be the most efficient at slowing down vacancies, and in this case the average V diffusivity is significantly slower than D_V only if $\Omega[X]z_{VX} > 1$, which is the same criterion as the one required to increase $[\bar{V}]^{\text{eq}}$.

We now want to derive an expression for F_R, which depends on temperature, irradiation flux, sink strength, and solute nominal concentration only. To this end, we proceed in three steps to compute all cluster concentrations in the system. First, we use the mass balance equation for solutes: $[\bar{X}] = [X](1 + \Omega[V]z_{VX} + \Omega[I]z_{IX})$. Second, we use Eq. (4) to express $[d]$ as a function of $[\bar{d}]$, which allows us to rewrite the nominal solute concentration as a function of total point-defect concentrations. Third, $[\bar{V}]$ and $[\bar{I}]$ are computed by solving Eq. (1) at steady state. The resulting total point-defect concentrations are functions of ϕ, k_V^2, k_I^2, T, and $[X]$. These analytical solutions are then used to obtain a single equation which allows us to find $[X] = f(T,\phi,k_V^2,k_I^2,[\bar{X}])$. Knowing $[X]$, all cluster concentrations and diffusivities are computed from previous relations.

To summarize, we identify two criteria that a solute must meet in order to increase F_R: $L_{VV}(VX) < D_V$ and $\Omega[X]z_{VX} > 1$. These criteria quantify the requirements that the solutes trap vacancies and that the resulting solute-vacancy clusters migrate more slowly than free vacancies, thus allowing for an efficient screening of candidate solutes (Sec. III A). Then, for a given solute, F_R is computed as a function of T, ϕ, k_V^2, k_I^2, and $[\bar{X}]$ knowing solute-point-defect binding energies and solute-point-defect cluster transport properties. The latter are computed in the SCMF framework, which requires solute-point-defect migration energies and attempt frequencies as an input. We compute all the atomic scale information using DFT.

B. Cluster transport coefficients

In the framework of the thermodynamics of irreversible processes, a flux of species α ($\vec{J}_\alpha$) is expressed as a linear combination of driving forces, i.e., chemical potential gradients of species β (μ_β),

$$\vec{J}_\alpha = -\sum_\beta L_{\alpha\beta}\vec{\nabla}\left(\frac{\mu_\beta - \mu_M}{k_B T}\right), \tag{8}$$

where $L_{\alpha\beta}$ are the transport coefficients and μ_M is the reference chemical potential for matrix atoms. Species α and β can be either solute X or point defect d. The off-diagonal transport coefficients ($\alpha \neq \beta$) are related to flux coupling phenomena.

As proposed in Ref. [39], the Onsager matrix can be split into cluster contributions and in the dilute limit, we consider the following clusters: isolated V, isolated I, isolated X, VX and IX pairs. The VI clusters are not considered because V and I spontaneously recombine below a certain distance such that $L_{IV} = L_{VI} = 0$ in Eq. (9). If mixed dumbbells (solute-matrix atom dumbbell) are unstable, solute atoms

cannot diffuse with a self-interstitial mechanism, such that $L_{IX} = L_{XI} = 0$, and IX clusters do not contribute to the L_{XX} transport coefficient. With these considerations in mind, the Onsager matrix is

$$\begin{pmatrix} L_{VV} & L_{VI} & L_{VX} \\ L_{IV} & L_{II} & L_{IX} \\ L_{XV} & L_{XI} & L_{XX} \end{pmatrix} = [V]\begin{pmatrix} L_{VV}(V) & 0 & 0 \\ 0 & 0 & 0 \\ 0 & 0 & 0 \end{pmatrix} + [I]\begin{pmatrix} 0 & 0 & 0 \\ 0 & L_{II}(I) & 0 \\ 0 & 0 & 0 \end{pmatrix} + [IX]\begin{pmatrix} 0 & 0 & 0 \\ 0 & L_{II}(IX) & 0 \\ 0 & 0 & 0 \end{pmatrix} + [VX]\begin{pmatrix} L_{VV}(VX) & 0 & L_{VX}(VX) \\ 0 & 0 & 0 \\ L_{XV}(VX) & 0 & L_{XX}(VX) \end{pmatrix}, \tag{9}$$

where $L_{\alpha\beta}(\gamma)$ is the $\alpha\beta$ component of the Onsager matrix related to cluster γ (in m^2/s). Note that isolated solutes do not contribute to the Onsager matrix because they cannot diffuse on their own and need to pair with a defect. Equation (9) makes it clear that flux coupling only comes from VX clusters (nonzero off-diagonal transport coefficients). The qualitative nature of flux coupling (either positive or negative) is thus given by the VX pair drag ratio $L_{XV}(VX)/L_{XX}(VX)$. The full kinetic properties of such system are reduced to six cluster transport coefficients which are intrinsic and equilibrium properties of each cluster: $L_{VV}(V)$, $L_{II}(I)$, $L_{VV}(VX)$, $L_{VX}(VX)$, $L_{XX}(VX)$, and $L_{II}(IX)$. Once these quantities are computed at each temperature, the full Onsager matrix of the dilute system can be obtained for any cluster concentrations.

The self-consistent mean-field theory (SCMF) [49,50] computes the cluster transport coefficients from atomic jump rates. First developed for vacancy-mediated diffusion [37,38,51–53], it has been extended to split dumbbell [54,55] and interstitial impurity migration [39]. Besides providing the full Onsager matrix, the SCMF method also enables a controlled tuning of the approximation of kinetic correlations, whereas in the well-known five-frequency model [56–58], kinetic correlations are computed to first order only, which is not always sufficiently accurate [37,38]. Technical details about the SCMF method can be found in Refs. [38,39,50]. In short, the SCMF method performs a statistical average over all possible trajectories within a local volume, determined by the correlation radius R_{cor}. The larger R_{cor}, the more precise the estimation of kinetic correlations, but also the more computationally expensive. Usually, setting R_{cor} equal to a few nearest-neighbor (NN) distances is sufficient to obtain transport coefficients converged to within less than ~10% [38,39]. In this study, $R_{\text{cor}} = 2.5a$ for VX transport coefficients. Cluster transport coefficients for V, I, and IX are simple enough to be computed without using the SCMF method.

III. MODELING RESULTS

A. Screening solute candidates in Cu

As an application of the multiscale framework presented in Sec. II, we identify candidate solutes able to trap and slow down vacancies in a Cu solid solution using available high-throughput DFT data where migration energies were computed for 40 substitutional solutes [58]. Following the developments of Sec. II A, candidate solutes should meet two criteria: $\Omega[X]z_{VX} > 1$ and $L_{VV}(VX) < D_V$. The first one is to have sufficient binding energy with V. In Ref. [58], only 1NN V-X interactions were considered, such that the cluster partition function is expressed as $z_{VX} = 12\exp(E_b(VX_1)/k_BT)$, and the "1" subscript denotes the microscopic configuration of the VX pair where V and X are 1NN from each other. Hence the first criterion is expressed in a more convenient form:

$$E_b(VX_1) > -k_BT\ln(12\Omega[X]). \tag{10}$$

As an example, the right-hand side is ≃0.23 eV at $T = 600$ K and $\Omega[X] = 0.1$ at.%. The five-frequency model [56,57] used to compute solute diffusivities in Ref. [58] does not give the $L_{VV}(VX)$ coefficient. If we assume that both species V and X diffuse at the same speed when they form a cluster (i.e. the VX cluster never dissociates), then $L_{VV}(VX) \simeq L_{XX}(VX)$, where $L_{XX}(VX)$ corresponds to the diffusivity of the VX cluster. The average V diffusivity obtained this way is similar to previous expressions [45,47,48]. This assumption breaks down at high temperature and/or when the VX binding energy is small, because V often dissociates from X (see Sec. III C). The equilibrium solute diffusivity can be expressed as $D_X^{\text{eq}} = \Omega[V]^{\text{eq}}z_{VX}L_{XX}(VX)$. When this solute is taken to be a matrix tracer atom (Cu in our case), then the self-diffusion coefficient is directly related to the vacancy diffusivity: $D_{\text{Cu}}^{\text{eq}} = \Omega[V]^{\text{eq}}f_0D_V$, where $f_0 = 0.78146$ is the tracer correlation coefficient for FCC systems [59]. Using these two assumptions, $\bar{D}_V$ can be estimated from available experimental [60] and/or modeling [58] values for the solute equilibrium diffusivity and matrix self-diffusion coefficient. Therefore the second criterion for identifying solutes that can slow down the diffusion of vacancies (compared with pure Cu) is

$$\bar{D}_V < D_V \Longrightarrow \frac{f_0D_X^{\text{eq}}}{z_{VX}D_{\text{Cu}}^{\text{eq}}} < 1. \tag{11}$$

Figure 1 plots these two criteria [Eqs. (10) and (11)] against each other for 40 different solutes in Cu. The plot is shown at $T = 600$ K but is qualitatively similar for other temperatures. Candidate solutes to increase F_R should be located in the shaded area (low diffusivity and high binding energy). The most promising solute that meets both criteria is Sb with $E_b(VSb_1) = 0.33$ eV and $f_0D_{\text{Sb}}^{\text{eq}}/z_{V\text{Sb}}D_{\text{Cu}}^{\text{eq}} \simeq 0.02$. The high binding energy between Sb and V obtained from DFT calculations [58] is in qualitative agreement with interdiffusion experiments in this system [61]. Other possible candidate solutes are Tl, Pb and Bi because they have a higher binding energy than Sb, although they do not slow vacancies as effectively as Sb atoms. These three solutes, however, have a rather low solubility limit in Cu: for instance at $T = 600$ K,

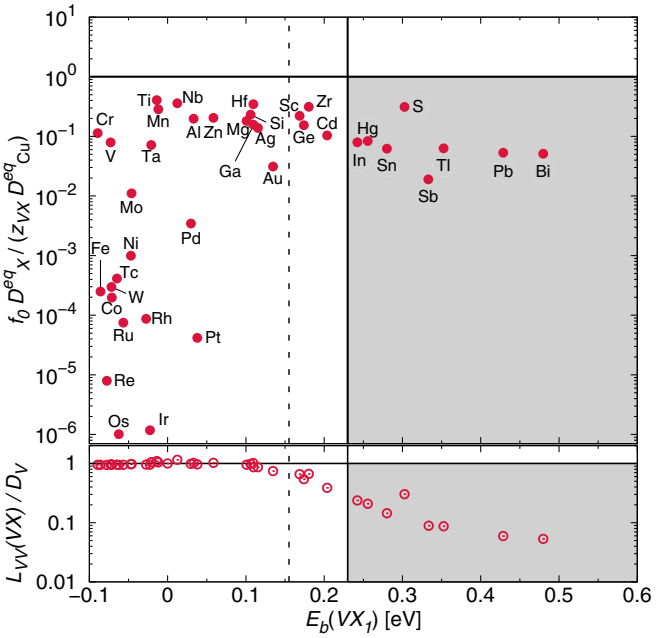

FIG. 1. $f_0 D^{eq}_X/(D^{eq}_{Cu} z_{VX})$ evaluated at $T = 600$ K and plotted as a function of the VX binding energy. $z_{VX} = 12\exp(E_b(VX_1)/k_BT)$ because only 1NN interactions are taken into account. According to the plot, all solutes are able to slow down vacancies, but the $L_{VV}(VX) = L_{XX}(VX)$ assumption underestimates $L_{VV}(VX)$ for solutes showing a low binding energy with V. This is further evidenced by the bottom part of the figure where $L_{VV}(VX)$ was computed using the SCMF method with the migration energy input from the five-frequency model [58]. Solutes showing a high enough attractive interaction with V [Eq. (10)] are those to the right of the vertical black line. Hence candidate solutes to increase F_R are found in the gray shaded area.

solubility limits amount to 0.0003 at.% [62], 0.008 at.% [63], and 0.0008 at.% [64] for Tl, Pb, and Bi, respectively, while the Sb solubility limit is 2.7 at.% [65]. Thus, using Sb over Tl, Pb, or Bi allows larger amounts of solutes without introducing thermodynamic driving forces for solute precipitation. Note that irradiation can increase or decrease solubility limits [66]. Nevertheless, the equilibrium solubility limit of Sb is at least two orders of magnitude higher than that of Tl, Pb and Bi, such that the Sb content of the solid solution under irradiation is expected to be the highest among these solutes. In, Hg, Sn, and S also meet both criteria, but they have a lower binding energy with V than Sb, and they do not slow down V as effectively. Hence these solutes would be less effective than Sb at increasing F_R.

It is important to keep in mind that we assumed $L_{VV}(VX) = L_{XX}(VX)$ while in reality $L_{VV}(VX) \geqslant L_{XX}(VX)$. In fact, the $L_{VV}(VX)$ coefficient of solutes with a binding energy lower than $2 - 3k_B$ can be underestimated by orders of magnitude. In other words, Eq. (11) only enables to rule out solutes that will not increase F_R. This statement is evidenced in the bottom part of Fig. 1, where the $L_{VV}(VX)$ coefficients for each solutes have been computed using the five-frequency input from Ref. [58] in the SCMF method. Hence for solutes that verify both Eqs. (10) and (11), a quantitative calculation of $L_{VV}(VX)$ must be performed to guarantee that they would indeed increase F_R. The approximate criterion in Eq. (11) aims at making the identification of candidate solutes easy-to-use from existing diffusion data, and it is a good approximation for solutes with sufficient binding energy, which are the only ones of real interest here.

The choice of candidate solutes relies on V-X interactions only because I-X interactions do not affect F_R unless $\bar{D}_I \leqslant \bar{D}_V$. Previous studies emphasize the need to trap self-interstitials instead of vacancies [29,32,33], but Eq. (2) shows that as long as self-interstitial atoms diffuse much faster than vacancies, the total concentration of vacancies governs the recombination rate. In the case where self-interstitials are immobile when they are trapped by a solute and vacancies are not slowed down by these solutes, we derive a first-order criterion for vacancies to diffuse faster than self-interstitials,

$$\bar{D}_V > \bar{D}_I \Longleftrightarrow E_b(IX) > E_m(V) - E_m(I), \qquad (12)$$

where the migration energies are those of isolated point defects diffusing in a bulk system. This expression is similar to the one obtained by Mansur *et al.* [31]. For Cu, this would require a very high binding between the solute and the self-interstitial $E_b(IX) > 0.60$ eV, whereas $E_b(I\text{Sb}) \simeq 0.18$ eV (see Appendix C). If vacancies are indeed faster diffusers than self-interstitials, the whole analysis presented in Sec. II A remains valid, except that z_{IX} and $\bar{D}_I$ would be the quantities of interest instead of z_{VX} and $\bar{D}_V$. Combining two different solutes, one to trap vacancies and the other to trap self-interstitials, would only be useful if the average diffusivities of both defects were similar.

B. Density functional theory calculations

Figure 1 shows that the solute that can most efficiently increase the fraction of recombined point defects in irradiated Cu is Sb, but in Ref. [58] diffusivities have been calculated in the five-frequency framework which is not always accurate as it neglects interactions beyond the 1NN configuration. Moreover, there are no available data for ISb interactions. We thus perform additional density-functional theory (DFT) calculations to compute the atomistic quantities (binding and migration energies) needed to obtain transport coefficients with the SCMF method. The detailed description of these calculations for the Cu(Sb) alloy is provided in Appendices C and D. Here we summarize the main results that are required for the following sections. We find an attractive binding energy between V and Sb for all configurations between 1NN and 9NN, the strongest being for the 1NN configuration: $E_b(VX_1) = 0.38$ eV. The VSb binding energy is lower than 0.08 eV for all other configurations. Migration barriers and attempt frequencies between all of these configurations are computed and given in Table I. The most stable self-interstitial configuration in pure Cu is a dumbbell oriented along a $\langle 100 \rangle$ direction, and the corresponding geometrical multiplicity is thus $z_I = 3$. The most probable dumbbell migration mechanism is a translation along [110] direction combined with a 90° rotation along [001]. CuSb mixed dumbbells are unstable and spontaneously relax to a configuration where the Sb solute is one lattice parameter away from the dumbbell. There are several attractive configurations between Sb and $I_{\langle 100 \rangle}$ dumbbell, the most stable one having a binding energy of 0.18 eV.

TABLE I. Migration data for dumbbell migration in pure copper and vacancy-mediated diffusion around a Sb atom. The first column is the label of the jump between configurations i (initial) and f (final), see Fig. 6. Saddle-point energies are given as the binding energy at the saddle-point position $E^d_{sp}(if) = E_b(dX_{if})$, see Eq. (C1). Migration energies are defined as $E_m(if) = -E^d_{sp}(if) + E_b(i)$ and $E_m(fi) = -E^d_{sp}(if) + E_b(f)$. All energies are in eV. Attempt frequencies ν^d_{if} are in THz, and have been computed using the one-atom (respectively, 21-atom) approximation of Vineyard transition state theory for V (respectively, I).

Jump	i	f	$E^d_{sp}(if)$	$E_m(if)$	$E_m(fi)$	ν^d_{if}
ω^I_0	∞	∞	–0.128	0.128	0.128	2.35
ω^V_0	∞	∞	–0.717	0.717	0.717	3.47
ω^V_{ex}	1	1	–0.092	0.473	0.473	7.26
ω^V_{11}	1	1	–0.564	0.945	0.945	4.68
ω^V_{12}	1	2	–0.449	0.830	0.508	5.10
ω^V_{13}	1	3	–0.424	0.805	0.433	5.32
ω^V_{14}	1	4	–0.366	0.747	0.401	5.22
ω^V_{23}	2	3	–0.733	0.793	0.742	5.16
ω^V_{25}	2	5	–0.614	0.673	0.643	5.03
ω^V_{33}	3	3	–0.690	0.699	0.699	4.86
ω^V_{34}	3	4	–0.767	0.776	0.802	4.83
ω^V_{35}	3	5	–0.667	0.676	0.697	4.96
ω^V_{36}	3	6	–0.728	0.737	0.752	5.01
ω^V_{37}	3	7	–0.708	0.717	0.722	5.01
ω^V_{45}	4	5	–0.630	0.665	0.660	4.88
ω^V_{47}	4	7	–0.711	0.746	0.725	4.95
ω^V_{48}	4	9	–0.674	0.709	0.694	4.94

Because mixed dumbbells are unstable, Sb atoms will not diffuse with a self-interstitial mechanism and act as immobile traps for this defect. Therefore it is not necessary to compute the migration barriers between all Sb$I_{\langle 100\rangle}$ configurations.

C. Average point defects diffusivities

The data obtained with DFT (see Appendices C and D) informs the SCMF method, allowing us to compute the six cluster transport coefficients identified in Eq. (9). The coefficients $L_{VV}(V)$ and $L_{II}(I)$ are the diffusivities of isolated point defects in pure Cu: $L_{VV}(V) = a^2\nu^V_0 \exp(E^V_{sp}(\infty\infty)/k_BT)$ and $L_{II}(I) = \frac{2}{3}a^2\nu^I_0 \exp(E^I_{sp}(\infty\infty)/k_BT)$, where the $\frac{2}{3}$ factor accounts for the anisotropy of the $\langle 100\rangle$ dumbbell diffusion [23]. The vacancy diffusivity in pure Cu is plotted as a green line in Fig. 2. The coefficients $L_{VV}(V\text{Sb})$, $L_{V\text{Sb}}(V\text{Sb})$ and $L_{\text{SbSb}}(V\text{Sb})$ are directly obtained from the SCMF method applied to a VSb cluster using the data from Fig. 7 and Table I. We did not compute the $L_{II}(I\text{Sb})$ coefficient to the same level of accuracy because we know from the rate theory analysis in Sec. II A that the average self-interstitial diffusivity does not impact the fraction of recombined point defects as long as I diffuses much faster than V. A rough estimation of $L_{II}(I\text{Sb}) \simeq L_{\text{SbSb}}(I\text{Sb}) = 0$ is thus sufficient for our study, while a comprehensive calculation would require a large set of DFT data (all migration barriers of the dumbbell around a solute).

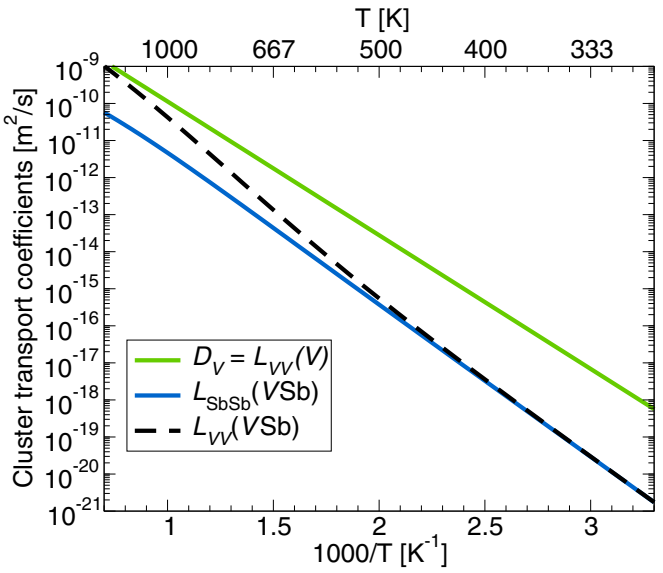

FIG. 2. VSb cluster transport coefficients obtained with the SCMF method, using data from Table I and Fig. 7. The green line shows the diffusivity of isolated vacancies, and the blue line shows the diffusivity of a VSb pair (without dissociation). Both of them follow an Arrhenius law. The $L_{VV}(V\text{Sb})$ coefficient is plotted as a black dashed line, and corresponds to the average diffusivity of a vacancy inside a cluster, considering both long-range migration with the solute and association/dissociation jumps.

The effect of Sb on the kinetic properties of V stems from two intertwined mechanisms: long-range VSb diffusion, and successive associations/dissociations of V with/from Sb. The long-range migration of VSb clusters is limited by the ability of the solute to diffuse, and this contribution is plotted as a blue line in Fig. 2. An Arrhenius fit to the cluster diffusivity gives $L_{\text{SbSb}}(V\text{Sb}) = 3.21 \times 10^{-8} \exp(-0.807/k_BT)$. The vacancy can also dissociate from the solute, with low or high rate depending on the solute and temperature. Dissociation jumps do not contribute much to the overall V diffusivity at low temperature because the binding energy between V and X produces a deep energy basin from which it is hard to escape. At high temperature, the trapping basin becomes more shallow and the lifetime of a VX cluster is reduced, i.e., once the pair is formed, V is more likely to dissociate from the solute than diffuse with it over extended periods of time. The diffusivity of V around Sb is given by the coefficient $L_{VV}(V\text{Sb})$, plotted as a black dashed line in Fig. 2. As expected, it goes from the VSb pair diffusivity at low temperature to the diffusivity of an isolated vacancy at high temperature. Indeed, at high temperature, all configurations where V is located around the solute have similar energies, so V does not feel the presence of the solute and diffuses as if it was isolated in the bulk.

D. Effect of Sb on the fraction of recombined point defects

In this section, we present a quantitative assessment of the effect of Sb addition to a Cu solid solution, using the fraction of recombined point defects as a measure of the efficiency of Sb. The fraction of recombined point defect is computed using the homogeneous rate theory model developed in Sec. II A, where thermodynamic and kinetic information is derived from

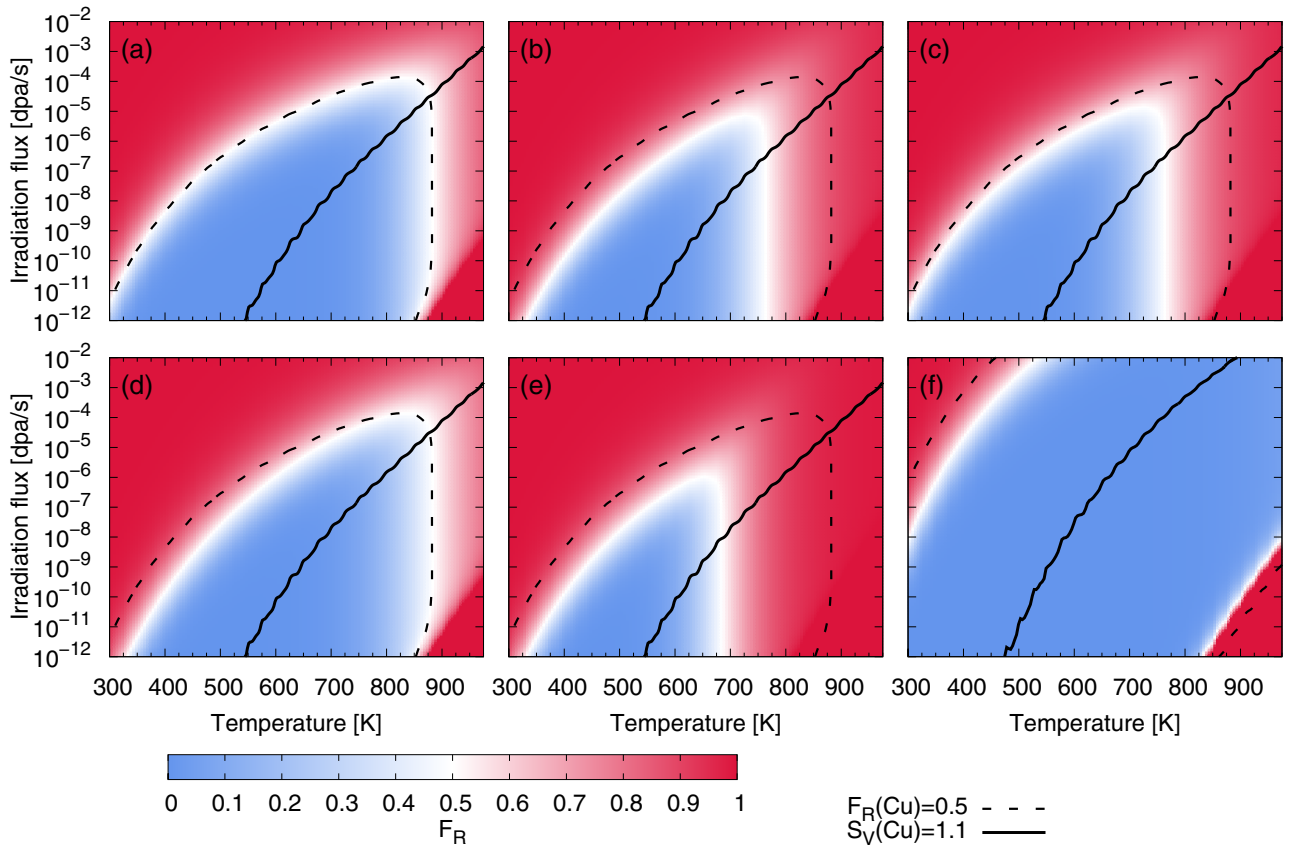

FIG. 3. Fraction of recombined point defects [Eq. (2)] as a function of irradiation rate ϕ and temperature T. The solid line shows the contour at which the vacancy supersaturation is 1.1 in pure Cu: $S_V = [V]/[V]^{\mathrm{eq}} = \exp\left(\frac{\mu_V - \mu_V^{\mathrm{eq}}}{k_B T}\right) = 1.1$. (a) is the reference plot for pure Cu with a sink strength $k^2 = 10^{14}$ m^{-2}, and the dashed line (copied on each plot) corresponds to $F_R = 0.5$; (b) is obtained by adding 1 at.% Sb to the system, all other parameters being held as in (a). (c) The migration energy of VSb clusters was decreased by 0.10 eV, making the diffusion of VSb pairs similar to that of isolated vacancies. (d) and (e) Solute concentration is changed to 0.1 and 5 at.%, respectively. (f) shows the evolution of F_R when the sink density increases to $k^2 = 4 \times 10^{16}$ m^{-2}. Note that a change in sink strength also affects F_R and S_V in pure Cu.

the atomic scale, as presented in Secs. III B and III C. Remaining free parameters in the model correspond to irradiation conditions (ϕ, T), microstructure (assuming unbiased sinks $k_V^2 = k_I^2 = k^2$) and solute nominal concentration [$\bar{X}$].

Figure 3(a) shows the fraction of recombined point defects F_R in pure Cu as a function of irradiation rate and temperature, and two regimes are identified: recombination and elimination at sinks. The dashed line corresponds to the $F_R = 0.5$ contour, defining a region inside of which most point defects are eliminated at sinks (blue region), and outside of which most point defects recombine (red region). The solid line corresponds to a vacancy supersaturation of 10%, meaning that V supersaturation should not be a significant issue below this line (high temperature and low irradiation flux region). Both lines, computed in pure Cu, are added as references to the other plots [Figs. 3(b)–3(f)]. For a given temperature, as the irradiation flux increases, F_R increases because the concentration of point defects in the Cu matrix increases, and a vacancy has more chance to meet a self-interstitial atom on its way to sinks (and conversely). At fixed irradiation rate, F_R first decreases with temperature because, as seen in Eqs. (2) and (3), F_R is a decreasing function of the vacancy diffusion coefficient which increases with temperature. This statement holds as long as $[V]^{\mathrm{eq}} \ll \phi/\Omega k^2 D_V$ and $[V]^{\mathrm{eq}} \ll k^2/4\pi r_c$. For $\phi = 10^{-6}$ dpa s^{-1}, $r_c = a\sqrt{3}$ [67], $k^2 = 10^{14}$ m^{-2} (which corresponds for instance to a 350 nm thick thin-film or a grain 600 nm in diameter), and taking the experimental value of the vacancy formation energy $E_f(V) = 1.28$ eV [68,69], both relations are true up to $T = 736$ and 944 K, respectively. At high temperature where $[V]^{\mathrm{eq}}$ is comparable to the concentration of V created by the irradiation flux, solving Eq. (1) gives $[V] \simeq [V]^{\mathrm{eq}}$. Thus F_R increases with increasing temperature. This behavior is expected because when the equilibrium point-defect concentrations reaches a high level, it becomes difficult to create point-defect supersaturations, hence the driving force for elimination at point-defect sinks is very low. In summary, there are two successive mechanisms contributing to the temperature evolution of F_R at fixed irradiation flux: at low temperature, the total vacancy concentration is governed by the vacancy diffusivity, and thus decreases with increasing temperature. At high temperature, the total vacancy concentration is governed by the equilibrium vacancy concentration, and thus increases with increasing temperature.

Figure 3(b) shows that a 1 at.% Sb addition enlarges the point-defect recombination regime and comparison with Figs. 3(c)–3(e) reveals two distinct mechanisms that are responsible for the increase in F_R. Compared with the model that

was used to obtain Fig. 3(a), all parameters are kept identical in Fig. 3(b), but 1 at.% Sb was added, and thermodynamic and kinetic data are taken from previous sections. These two mechanisms are clearly revealed by varying some of the parameters. In Fig. 3(c), the migration energy of VSb clusters is decreased by 0.1 eV, which means that these clusters diffuse as fast as isolated vacancies (instead of being slower as in Fig. 3(b). The beneficial effect of Sb addition disappears at low temperature, where the $F_R = 0.5$ contour matches that of pure Cu. Yet, the beneficial effect of Sb addition at high temperature remains unaffected by the VSb cluster migration energy decrease since at high temperature, F_R is governed by the total equilibrium vacancy concentration.

Figures 3(d) and 3(e) show that upon nominal Sb concentration changes, only the high temperature boundaries of the recombination domain are affected. These plots are obtained using the same parameters as in plot 3(b) except that the nominal Sb concentration is changed to 0.1 and 5 at.%, respectively. We see that the low-temperature region where F_R is increased by the presence of Sb is not affected by this change. This is because at low temperature the $z_{V\mathrm{Sb}}$ term [related to binding energies, cf. Eq. (5)] is large enough such that $z_{V\mathrm{Sb}}[\mathrm{Sb}]\Omega \gg 1$ even for $[\mathrm{Sb}]\Omega = 0.001$. The average vacancy diffusivity in Eq. (7) becomes $\bar{D}_V \simeq L_{VV}(V\mathrm{Sb})$ and thus does not depend on the solute concentration or the solute-vacancy binding energy. In other words, most vacancies are paired with solutes and we can neglect the contribution of isolated vacancies in the average thermodynamic and kinetic properties of the vacancy population. Nevertheless, a change in solute concentration affects the high temperature region around $T = 800$ K. For low Sb concentration [Fig. 3(d)] the effect of Sb in this region disappears, which means that the total equilibrium vacancy concentration is similar to that of pure Cu: $z_{V\mathrm{Sb}}[\mathrm{Sb}]\Omega \ll 1$. On the other hand, when the solute concentration increases [Fig. 3(e)] the presence of Sb widens the region of high F_R because it stabilizes vacancies in the solid solution and increases the total equilibrium vacancy concentration. Note that what matters in these expressions is not the nominal solute concentration alone but the product $z_{V\mathrm{Sb}}[\mathrm{Sb}]\Omega$, such that increasing the vacancy-solute binding energy will have qualitatively the same effect as increasing the solute concentration.

Lastly, we show that the widening of the recombination domain upon Sb addition also occurs at higher sink strength. In Fig. 3(f), the sink strength is increased from $k^2 = 10^{14}$ m^{-2} to $k^2 = 4 \times 10^{16}$m^{-2} (the latter corresponds to an average grain diameter of 30 nm). All other parameters are set to the same values as in Fig. 3(b). Note that the pure Cu reference lines (dashed and solid black lines) are shifted compared with the other plots because they also depend on the sink strength. Due to the sink strength increase, the sink elimination domain is larger than in previous cases, but the addition of Sb is still able to reduce the extent of this domain (compared with pure Cu) in the low-temperature/high flux region by slowing down vacancies.

E. Long-term stability of the solid solution

As indicated in the introduction, solute-defect flux coupling raises the question of the long term stability of a solid solution such as Cu(Sb). Indeed, in case of a positive flux coupling (drag), solutes will be continuously driven towards sinks, reducing the bulk solute concentration and hence decreasing F_R. Note that in the recombination regime ($F_R \simeq 1$), point-defect fluxes to sinks are low, but still nonzero, hence the addition of solutes with positive flux coupling would only be beneficial for a finite irradiation dose. Moreover, solute segregation to sinks might cause mechanical issues, e.g., grain boundary embrittlement [18,19]. Yet, if most point defects recombine in presence of Sb, this solute redistribution process might be very slow, and may be sufficiently slow compared to the lifetime of the material. In the case of negative flux coupling between point defects and solutes, F_R should theoretically increase over time as the concentration of Sb atoms in the solid solution will increase.

We now show that despite having positive flux coupling coefficients between V and Sb, there is a temperature range where point-defect trapping by Sb is efficient while flux coupling coefficients are low. Knowing point-defect solute binding energies, we estimate $F_T(d)$, the fraction of trapped point defects in the system, as a function of solute concentration and temperature. For dilute solid solutions obeying local equilibrium, $F_T(d)$ is independent of the point-defect concentration

$$F_T(d) = \frac{[dX]}{z_d[d] + [dX]} = \frac{1}{1 + \frac{z_d}{\Omega[X]z_{dX}}}. \tag{13}$$

In the Cu(Sb) system, mixed Cu-Sb dumbbells are not stable meaning that self-interstitial atoms will not produce any solute redistribution. Thus, only vacancies create flux coupling, and the VSb drag ratio is positive up to $T = 1188$ K. For simplicity, we assume $\nabla(\mu_X - \mu_{\mathrm{Cu}}) = 0$, which would correspond to the beginning of irradiation of a homogeneous solid solution, and the flux of solutes is directly proportional to the flux of V:

$$\begin{aligned}\frac{J_X}{J_V} &= \frac{[VX]L_{XV}(VX)}{[V]L_{VV}(V) + [VX]L_{VV}(VX)} \\ &= \frac{\eta_{VX}}{1 + \frac{[V]L_{VV}(V)}{[VX]L_{VV}(VX)}} \\ &= \frac{\eta_{VX}}{1 + \frac{L_{VV}(V)}{\Omega z_{VX}[X]L_{VV}(VX)}},\end{aligned} \tag{14}$$

where $\eta_{VX} = L_{XV}(VX)/L_{VV}(VX)$ is the VX pair cluster flux coupling coefficient. Broadly speaking, it is the maximum efficiency of solute redistribution for a given vacancy flux, i.e., when all vacancies are paired with solute atoms and when there are no solute chemical potential gradients. Knowing that a large majority of vacancies may form VSb pairs (assuming that the Sb concentration is large enough and that the temperature is low enough), η_{VX} is a good approximation of the flux ratio between solutes and vacancies, and its temperature evolution is plotted as a blue curve in Fig. 4. The black curves show how this flux ratio evolves with two solute concentrations: $[\mathrm{Sb}] = 0.1$ at.% and $[\mathrm{Sb}] = 1.0$ at.%. Figure 4 also shows the fraction of trapped vacancies $F_T(V)$ [Eq. (13)] for the same solute concentrations (red curves). It is interesting to note that both quantities $F_T(V)$ and J_{Sb}/J_V decrease with temperature, but J_{Sb}/J_V decreases more rapidly than $F_T(V)$ as temperature increases. So increasing temperature reduces

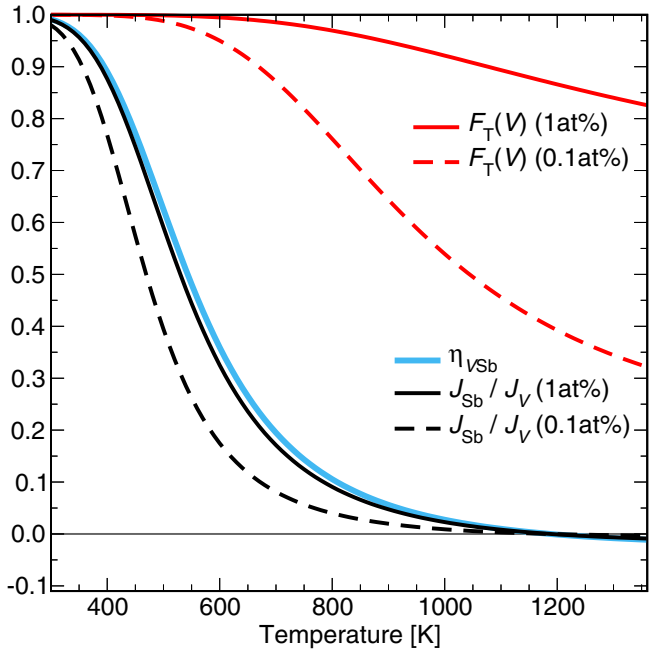

FIG. 4. Fraction of vacancies trapped by Sb solutes ($F_T(V)$, red curves) and flux ratio (J_{Sb}/J_V, black curves) given as a function of temperature. For solid and dashed lines, the Sb concentration is set to 1 and 0.1 at.%, respectively. The blue curve represents η_{VX}, which is the maximum flux ratio and only depends on the jump rates of V around Sb, not on the relative concentration of each species and defects.

flux coupling, while it can preserve a high fraction of trapped vacancies, ensuring that the Sb addition increases the fraction of recombined point defects over extended periods of time. For instance, there is a temperature window around 800 K, where η_{VX} is one order of magnitude lower than at room temperature while $F_T(V)$ is still high ($> 95\%$ when $\Omega[\text{Sb}] = 1$ at.%). When the solute concentration drops to 0.1 at.%, $F_T(V)$ is significantly reduced above $T = 600$ K, while the reduction of the flux ratio is less significant.

IV. DISCUSSION

We have shown that the effect of dilute solute additions on increasing the fraction of recombined point defect can be quantified combining DFT and SCMF with homogeneous rate equations. We identified two distinct mechanisms by which solutes such as Sb in Cu increase F_R: they trap and slow down vacancies at low temperature, while they stabilize vacancies in the solid solution at high temperature. Secondly, we have shown that there exists a temperature window where solute-enhanced recombination is significant while vacancy-induced solute drag remains very limited. This work therefore establishes that it is possible to design Cu-base solid solutions that are radiation resistant. We now discuss the validity of the main assumptions of the model, ideas for experimental validation and the applicability of this concept of radiation-resistant solid solution to other systems.

A. Modeling assumptions

An important simplifying assumption in our model is that we do not take into account point-defect clusters, neither those formed during displacement cascades nor the ones which nucleate on larger time scales. A first effect of point-defect clusters is that they will act as sinks and thus increase the sink strength over time, as discussed in Ref. [67]. Our dilute solid solution model would remain valid, except that with the sink strength increasing over time, F_R would progressively decrease for a given temperature and irradiation rate (see Fig. 3). The effect of solutes on the nucleation and growth of point-defect clusters is more difficult to foresee but several points are worth mentioning: (1) we checked that despite the increase of point-defect concentrations in the presence of solutes, point-defect chemical potentials are mostly identical to those in pure Cu, such that the presence of solutes does not increase the driving force for point-defect clustering; (2) we anticipate that solutes will act as nucleation centers due to the attractive binding between solutes and point defects, lowering the critical cluster size calculated in the framework of classical nucleation theory [70]; and (3) solutes lower the mobility of point defects, thus they should increase the incubation time and slow down the growth process.

The modeling of such systems can be improved by going beyond the homogeneous rate theory equations, to take into account the spatial distribution and time evolution of sinks, the precipitation of solutes and point-defect clusters, as well as solute and point-defect concentration inhomogeneities and fluxes. These improvements are beyond the scope of the present work, but cluster dynamics [71] or phase-field methods [72] can in principle deal with the complexity required to model these phenomena.

B. Experimental validation

The predictions obtained in this work could be validated, for instance, by irradiating thin films sandwiched between two buffer layers chosen so that the buffer/thin film interfaces would be effective sinks for point defects. For a Cu-based material as considered here, it has been showed by Mao *et al.* [73] that Nb/Cu interfaces in films grown by physical vapor deposition possess a high sink efficiency. Furthermore, as done in the above reference, measuring the broadening of a marker layer as a function of the irradiation dose would provide a direct determination of the vacancy supersaturation. Lastly, the solute drag predictions could be validated by monitoring the solute concentration in the film and at the Cu/buffer layer interfaces as a function of the irradiation dose.

C. Application to other systems

Now that we have shown that dilute solute additions to a solid solution can increase the fraction of recombined point defects in Cu, we briefly discuss the applicability of this concept to other FCC alloys, namely, Al and Ni. Diffusivity data computed with DFT is also available for these two systems [58] and we apply the same methods as in Sec. III A to identify candidate solutes. The results are plotted in Fig. 5 and solutes, which slow down vacancies and form substantial amounts of VX pairs at $T = 600$ K with solute concentrations of 0.1 at.%

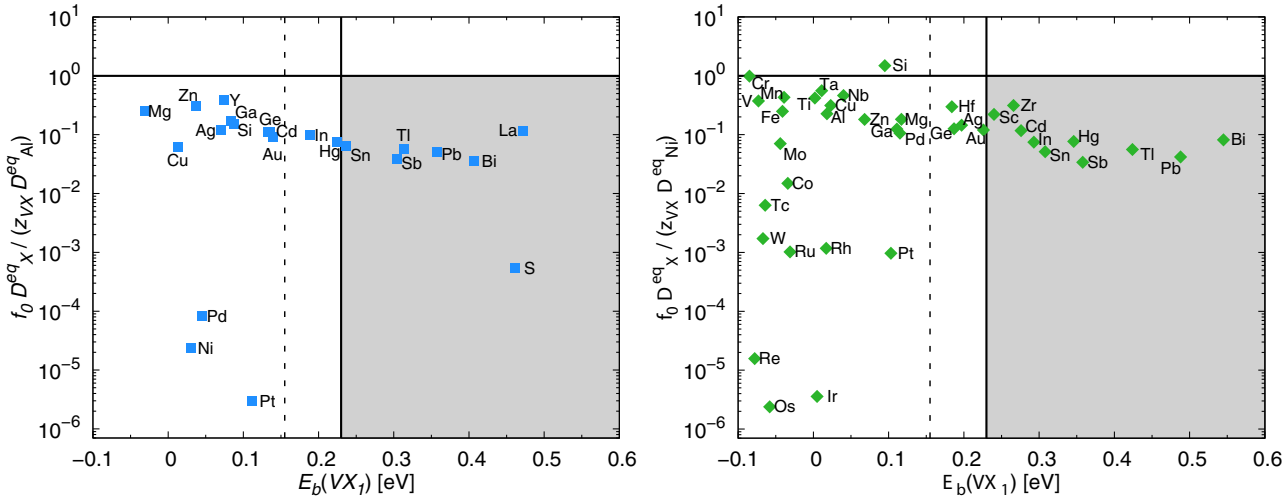

FIG. 5. The criterion in Eq. (11) is plotted against the 1NN vacancy-solute binding energy for two FCC matrices: Al (left) and Ni (right). Solutes which trap a non-negligible fraction of vacancies are located to the right of the vertical black line, and all solutes shown here could eventually slow down V. All the quantities are calculated at $T = 600$ K.

are located in the gray shaded area. The results presented in Sec. III D should then be transferable, at least qualitatively, to these other systems. For instance, S appears to be of interest for increasing the recombined fraction of point defects in Al as it combines a low diffusivity and a high binding. Moreover, it is noteworthy that some solutes, e.g., Sb or Tl, will be effective in increasing F_R in all three matrices. We recall that the ratio plotted in Fig. 5 is not a good approximation for solutes with a binding energy lower than $2 - 3k_B$, see the bottom part of Fig. 1.

An interesting strategy to further increase F_R would consist in combining different solutes, e.g., a first solute with a high binding energy for high temperatures, and a second solute with intermediate binding energy but slow diffusivity for lower temperatures. This idea stems from the identification of two distinct mechanisms to increase F_R by dilute solute additions (see Sec. II A). Alternatively, solute atoms showing attractive interactions when they simultaneously neighbor a vacancy would also be a promising solution to increase F_R since these three-body clusters with two substitutional solutes would probably diffuse much slower than an isolated vacancy. Currently, there is no database that would enable an efficient screening of the binding energy of these three-body clusters, and so testing this idea is beyond the scope of the present work.

V. CONCLUSION

This quantitative study confirms that adding specific solutes to a solid solution is indeed a viable concept to increase the fraction of recombined point defects under irradiation and thus reduce radiation damage. Unlike point-defect elimination at sinks, recombination is a local phenomenon that does not contribute to solute redistribution over a large scale. The effect of the solute is to slow down and stabilize point defects in the solid solution so as to increase the total concentration of point defects in the system and thus increase the probability that a vacancy recombines with a self-interstitial atom.

We presented a general framework that efficiently screens solute properties using existing diffusivity databases. Applied to a Cu matrix, this process identifies Sb as one of the most promising solute for increasing the fraction of recombined point defects F_R. We obtain quantitative thermodynamic and kinetic parameters of VSb and ISb clusters by combining DFT calculations with the SCMF method for transport coefficients. These parameters are then used in homogeneous rate theory equations to compute F_R as a function of temperature, irradiation rate, sink strength and solute concentration. From these results we identify two different mechanisms that come into play at various temperatures: provided that the binding energy between solute and vacancy is high enough at low temperature, the fraction of recombined point defects F_R is controlled by the ability of the solute to slow down vacancies. At higher temperatures where the total vacancy concentration under irradiation is similar to the equilibrium vacancy concentration, the ability of solutes to stabilize vacancies in the solid solution governs F_R. As long as self-interstitial atoms diffuse much faster than vacancies, the interactions between solutes and self-interstitial atoms do not affect F_R.

ACKNOWLEDGMENTS

Critical reading of the manuscript by members of the Trinkle research group is gratefully acknowledged. This research is supported by the U.S. Department of Energy (DOE), Offce of Science, Basic Energy Sciences (BES) under Award DE-FG02-05ER46217. This work made use of the Illinois Campus Cluster, a computing resource that is operated by the Illinois Campus Cluster Program (ICCP) in conjunction with the National Center for Supercomputing Applications (NCSA) and which is supported by funds from the University of Illinois at Urbana-Champaign.

APPENDIX A: DFT COMPUTATION DETAILS

Density-functional theory calculations are performed using the Vienna *ab initio* simulation Package (VASP) [74]. The

exchange and correlation energy is computed with the PBE generalized gradient approximation [75]. Copper ($[Ar]3d^{10}4s^1$) and antimony ($([Kr]4d^{10})5s^25p^3$) nuclei and core electrons are modeled by a projector augmented wave potential [76], as generated by Kresse and Joubert [77]. The plane-wave energy cutoff is set to 450 eV, which ensures energy convergence below 1 meV/atom. Calculations are performed on 108 ± 1 atoms supercells (depending on whether a vacancy or a self-interstitial atom is included) with a $6 \times 6 \times 6$ gamma centered k-point mesh. First-order Methfessel-Paxton smearing [78] with an energy set to 0.15 eV ensures accurate evaluation of forces for ionic relaxation. Binding energy calculations are relaxed with a conjugate gradient method, until the force on each ion is below 5 meV/Å. Migration energies are computed using the climbing image nudged elastic band method [79]. A single intermediate image is relaxed with a quasi-Newton scheme until the force on each ion is below 5 meV/Å. For vacancy-mediated jumps (respectively self-interstitial mediated jumps), attempt frequencies are computed in the one-atom [51,80,81] (respectively 21-atom) approximation of the Vineyard transition state theory framework [82]. With these DFT parameters, the computed Cu lattice parameter is $a = 3.629$ Å(3.615 Å [68]), the cohesion energy is $E_{\text{coh}}(\text{Cu}) = 3.727$ eV ($E_{\text{coh}}(\text{Cu}) =$ 3.49 eV [83]), and elastic constants are $C_{11} = 171.2$ GPa (169 GPa [84]), $C_{12} = 125.8$ GPa (122 GPa [84]) and $C_{44} =$ 76.7 GPa (75.3 GPa [84]). The values in parenthesis are from experimental measurements.

APPENDIX B: POINT-DEFECT FORMATION ENERGY IN PURE Cu

We compute point-defect formation energies in bulk Cu, which allow us to calculate the equilibrium concentration of these defects. The defect formation energy is defined as

$$E_f(d) = E[(\delta_d + n)\text{Cu} + d] - \frac{n + \delta_d}{n} E[n\text{Cu}], \quad \text{(B1)}$$

where $E[\alpha]$ is the total energy of a simulation box containing α, n is the number of Cu atoms in the supercell without defects or solutes ($n = 108$ in this study), and δ_d depends on the type of point defect: $\delta_V = -1$ and $\delta_I = +1$. The difference between the DFT V formation energy computed using Eq. (B1) ($E_f(V) = 1.036$ eV according to our calculations) and the experimental one ($E_f(V) = 1.28 \pm 0.05$ eV [68]) is due to anharmonicity effects [69]. We study the self-interstitial atom in an octahedral site and in three split dumbbell configurations oriented along the ⟨100⟩, ⟨110⟩ and ⟨111⟩ directions. The ⟨100⟩ split dumbbell configuration is the most stable configuration with formation energy $E_f(I_{\langle 100\rangle}) = 3.309$ eV, in agreement with previous studies [23,68]. The octahedral and ⟨110⟩ split dumbbell configurations are saddle-point configurations, with formation energies $E_f(I_{\text{oct}}) = 3.555$ eV and $E_f(I_{\langle 110\rangle}) =$ 3.814 eV, respectively. Both configurations spontaneously relax to the ⟨100⟩ configuration when one of the atoms is slightly displaced to break the symmetry of the configuration. We were not able to stabilize the ⟨111⟩ configuration which spontaneously relaxes to the ⟨110⟩ configuration. There are three possible $I_{\langle 100\rangle}$ orientations in the FCC crystal, such that the associated multiplicity is $z_I = 3$. For each type of point defect, the energy associated with the elastic interaction due to periodic images of defects was estimated using the ANETO code [85]. The corrected defect formation energies are $E_f(V) = 1.032$ eV, $E_f(I_{\langle 100\rangle}) = 3.177$ eV, $E_f(I_{\langle 110\rangle}) =$ 3.559 eV, and $E_f(I_{\text{oct}}) = 3.413$ eV. These corrections are small (∼5% for self-interstitials), which shows that our calculations are converged with respect to the supercell size.

APPENDIX C: SOLUTE-POINT-DEFECT BINDING ENERGIES

We compute the solute-point-defect binding energy for each symmetry unique configuration in a 108-atom supercell. The binding energy between defect d ($d = V$ or I) and solute X in microscopic configuration ρ is defined as

$$E_b(dX_\rho) = E[(n + \delta_d)\text{Cu} + d] + E[(n-1)\text{Cu} + X] - E[(n - 1 + \delta_d)\text{Cu} + dX_\rho] - E[n\text{Cu}]. \quad \text{(C1)}$$

In this paper, a positive binding energy denotes an attractive interaction between d and X.

The five-frequency model used in Ref. [58] considers all possible jumps from the 1NN VX configuration, and assumes all dissociation jumps to be equal [56,57]. In this study, we consider one additional thermodynamic shell, such that all jumps from a VX configuration belonging to the $(1\text{NN})^2$ shell (1NN of 1NN) are taken into account. As we want to distinguish between the various dissociation frequencies, we have to evaluate all stable configurations where V is located in the $(1\text{NN})^3$ shell of the solute. This sets the cut-off distance ρ_{VX} beyond which V and X are assumed to have no interaction: $\rho_{VX} = \sqrt{3}a$. For an isotropic defect such as the vacancy, there are eight possible configurations within the $(1\text{NN})^3$ shell. These eight VX configurations are uniquely defined by the distance between the vacancy and the solute, such that each microscopic configuration ρ of the pair is specified in terms of NN distance between V and X. The left part of Fig. 6 shows the position of the solute relative to the vacancy for each VX configuration, and these configurations are labeled from 1 to 9. Note that it is not possible to have a 8NN configuration in a 108-atom FCC cell because of periodic boundary conditions (the solute is then 2NN from a vacancy in a replica of the supercell). Moreover, this configuration does not belong to the $(1\text{NN})^3$ shell, even though it is closer to V than a 9NN site. To make it obvious that this configuration has not been calculated, it is denoted 8^* in Figs. 6 and 7.

Symmetry unique IX configurations cannot be distinguished by the point defect-solute distance only because the stable self-interstitial atom configuration is a split dumbbell configuration oriented along ⟨100⟩ directions of the FCC lattice which breaks the symmetry of the crystal. Hence solute positions that are symmetrically equivalent around V become distinct next to I. Let $\mathbf{u}_I$ be the unit vector parallel to the dumbbell orientation and $\mathbf{u}_X$ be the vector between the center of the defect and the solute, the latter being on a kNN site. We adopt the following nomenclature for IX configurations: if the largest component of $\mathbf{u}_X$ is along $\mathbf{u}_I$, then the configuration is denoted kp ("p" stands for parallel); if the smallest component of $\mathbf{u}_X$ is along $\mathbf{u}_I$, the configuration is denoted kn ("n" stands for normal); otherwise, the configuration is denoted

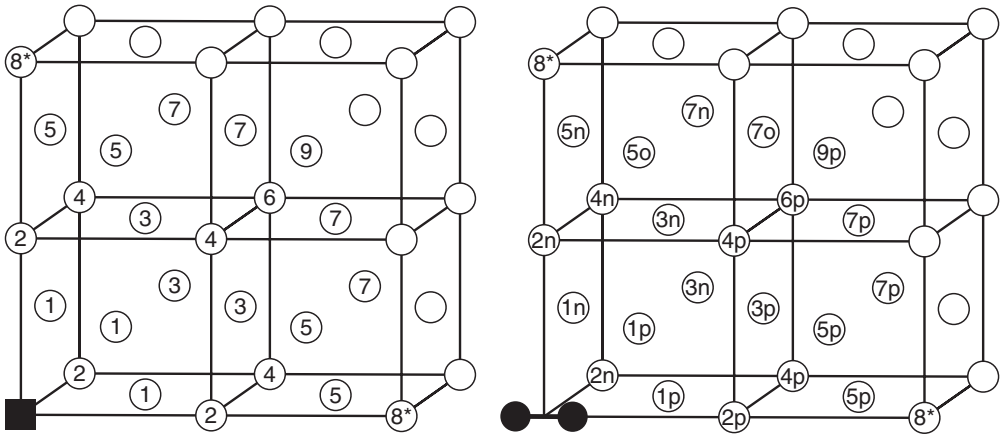

FIG. 6. Nearest-neighbor (NN) solute positions in the FCC lattice. The reference site is the one occupied by the defect: V (filled black square, left-hand plot) or I (filled black circles, right-hand plot). Because the ⟨100⟩ dumbbell configuration breaks the symmetry of the system, some solute positions that are symmetrically equivalent around V are distinct around I. These configurations are distinguished with a letter: "p," "o," or "n", depending on the orientation of the solute position vector with respect to the dumbbell orientation (see text). The 8NN configuration does not belong to the $(1NN)^3$ shell and has not been considered in this study; for this reason, it is identified as 8^*.

ko ("o" stands for other). A mixed dumbbell configuration (i.e. when the solute forms a dumbbell with a matrix atom) would be numbered 0, but it turns out that this configuration is unstable for Sb in Cu, and spontaneously relaxes toward a $2p$ configuration. This is not surprising considering that Sb is oversized in Cu. The 5NN and 7NN configurations are the only ones containing an "o" configuration, and 6NN orientations are all symmetrically equivalent, so the configuration is arbitrarily denoted $6p$.

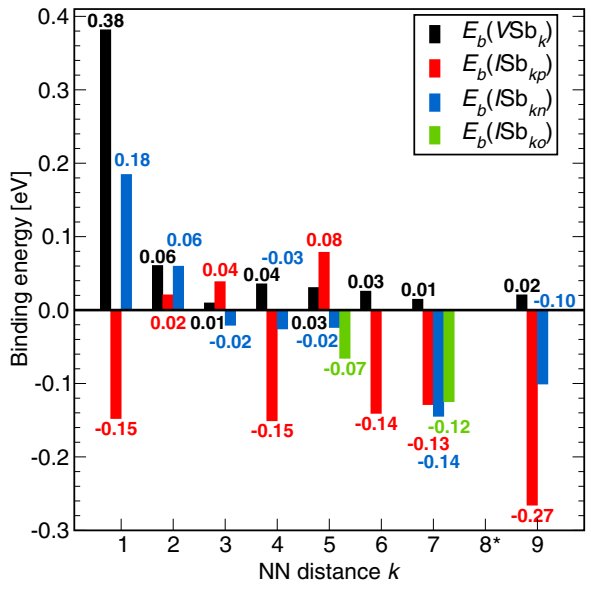

FIG. 7. Point defect (V or I) antimony binding energies [eV] obtained from DFT calculations. As defined in Eq. (C1), a positive binding energy corresponds to an attractive configuration. NN distances between d and X are shown in Fig. 6. Self-interstitial atoms have different possible orientations with respect to the solute, labeled either "p," "n," or "o" (see text). The 8NN configuration does not belong to the $(1NN)^3$ shell and has not been considered in this study; for this reason it is identified as 8^*.

Figure 7 shows the binding energy computed with DFT for all symmetrically unique solute configurations in the $(1NN)^3$ shell of a defect. The VSb binding is always positive (attractive) for these configurations, but the 1NN configuration is much more attractive then the other ones. The ISb binding is attractive at $1n$, $2n$, $2p$, $3p$, and $5p$ configurations, where $1n$ is the most attractive configuration, and the binding energy is about half of the VSb 1NN binding. Note that in the 5NN, 7NN, and 9NN configurations, the defect is between two solutes (i.e. located at half of the supercell size). The symmetry constraint that is imposed in this situation might not allow the configuration to relax as it would in a larger supercell. Practically, this should not have much effect if the solute-defect interaction is negligible at these distances, but large absolute values of binding energies obtained for these configurations should be considered with caution.

APPENDIX D: SOLUTE-POINT-DEFECT MIGRATION ENERGIES

We use DFT to identify the migration mechanisms of isolated point defects in pure Cu and compute the associated migration energies. Vacancies diffuse by exchanging with a 1NN Cu atom, and the corresponding migration energy is $E_m(V) = 0.717$ eV, in agreement with previous calculations [58,86,87] and experimental measurements $E_m(V) = 0.70 \pm 0.02$ eV [68]. The motion of the ⟨100⟩ split dumbbell defect is not so obvious, and we considered three mechanisms: translation to a 1NN site combined with a 90° in-plane rotation [Fig. 8(a)], translation to a 2NN site [Fig. 8(b)], and on-site 90° rotation perpendicular to the dumbbell orientation [Fig. 8(c)]. In Fig. 8, gray atoms represent the average positions (during the migration mechanism) of all atoms around the dumbbell in the (001) plane. Black and red atoms show the initial and final position and orientation of the dumbbell, respectively. Arrows emphasize the main atomic displacements during the migration of the dumbbell. The first mechanism [Fig. 8(a)] is the most probable one, with a migration energy

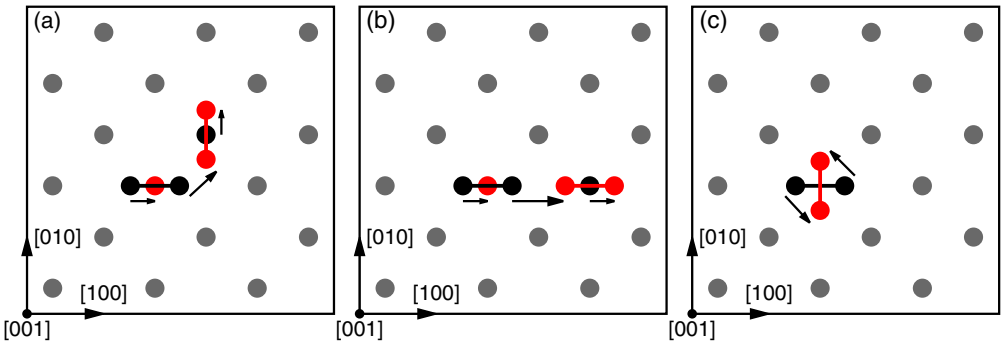

FIG. 8. Possible migration paths for $I_{[100]}$ in pure Cu: (a) translation of length $a/\sqrt{2}$ in the [110] direction combined with a 90° rotation about [001]; (b) translation of length a in the [100] direction; and (c) on-site 90° rotation about [001]. Only the (001) plane containing the defect is shown, and the bonds help to visualize the initial (black) and final (red) location of the dumbbell. Gray atoms show the averaged positions of atoms that are not directly involved in the migration mechanism.

$E_m^a(I) = 0.128$ eV (0.122 eV if we correct for elastic interactions between supercell replica [85]), in agreement with previous experimental estimations $E_m(I) = 0.117$ eV [68] and $E_m(I) = 0.125$ eV [29]. The saddle-point configuration for the second mechanism [Fig. 8(b)] corresponds to the self-interstitial atom being in an interstitial octahedral site. The migration energy is thus the formation energy difference between the ⟨100⟩ dumbbell configuration and the interstitial octahedral configuration, $E_m^b(I) = 0.246$ eV (0.236 eV with elastic correction). The third mechanism [Fig. 8(c)] is an on-site rotation, and the relaxed saddle-point configuration is a ⟨110⟩ dumbbell. The corresponding migration energy is thus $E_m^c(I) = 0.506$ eV (0.382 eV with elastic correction). There are other possible migration mechanisms where the saddle-point configuration is also a ⟨110⟩ dumbbell, e.g., translation in the [110] direction without rotation or with an out-of-plane rotation (90° rotation along [010]). These additional mechanisms all have the same migration energy. As the migration energy for the first mechanism [Fig. 8(a)] is at least 0.1 eV lower than the other two mechanisms, for simplicity, we only consider this first migration mechanism in our model.

We perform additional DFT calculations to understand vacancy migration paths in the presence of the Sb solute. We consider all the configurations shown in Fig. 6 and all symmetry unique transitions between them. There are 15 vacancy jumps (cf. Table I) to consider, and the vacancy jump frequency between the iNN and jNN configurations are denoted ω_{ij}^V (the three exceptions are the bulk jump rate ω_0^V, the V-Sb exchange rate ω_{ex}^V, and the bulk self-interstitial jump ω_0^I). Mixed dumbbells are unstable, such that there is no self-interstitial contribution to Sb transport and Sb acts as an immobile trap for I. As a first-order diffusion model, we do not take into account the details of I migration barriers around Sb, therefore only one I jump frequency appears in Table I.

For each symmetry unique jump in Table I, we also compute the attempt frequency, which requires a proper definition of the reference state for vibrational properties. In the SCMF method, transport coefficients are functions of products $p_i p_{i\to f} = p_f p_{f\to i}$, where i and f are two configurations of the system and the equality stems from detailed balance; p_i is the probability of being in configuration i and $p_{i\to f}$ is the probability to transition from configuration i to f:

$$\begin{aligned} p_i p_{i\to f} &\propto \exp\left(\frac{\mathcal{F}_b(Xd_i)}{k_B T}\right)\exp\left(-\frac{\mathcal{F}(Xd_{if}) - \mathcal{F}(Xd_i)}{k_B T}\right) \\ &= \exp\left(\frac{\mathcal{F}(X) + \mathcal{F}(d) - \mathcal{F}(Xd_{if}) - \mathcal{F}(\mathrm{Cu})}{k_B T}\right) \\ &= \exp\left(\frac{\mathcal{F}_{sp}^d(if)}{k_B T}\right) \\ &\simeq \nu_{if}^d \exp\left(\frac{E_{sp}^d(if)}{k_B T}\right), \end{aligned} \tag{D1}$$

where $\mathcal{F}(X)$, $\mathcal{F}(d)$, and $\mathcal{F}(\mathrm{Cu})$ are the free energies of isolated solute in Cu, isolated defect in Cu and pure copper, respectively. $\mathcal{F}(dX_{if})$ is the free energy of the saddle-point configuration between configurations i and f of the dX cluster. The last line of Eq. (D1) is approximate since we only take into account the vibrational entropy contribution of dX clusters, and ν_{if}^d is expressed as

$$\nu_{if}^d = \frac{\prod_{k=1}^{3n-3}\nu_k(d)\prod_{k=1}^{3n}\nu_k(X)}{\prod_{k=1}^{3n-4}\nu_k(dX_{if})\prod_{k=1}^{3n}\nu_k(\mathrm{Cu})}, \tag{D2}$$

where $\nu_k(\alpha)$ is the k^{th} eigenvalue of the force-constant matrix of a pure Cu lattice containing α [82]. For V, we compute the attempt frequencies in the one-atom or hoping atom approximation where we only consider a reduced force-constant matrix to estimate the most important eigenvalues [51,80,81]. For dumbbell migration in pure Cu the hopping atom approximation is not sufficient, because three atoms are involved in the migration mechanism [cf. Fig. 8(a)], and the surrounding atoms also undergo non-negligible ionic relaxation. In the end, 21 atoms (all 1NN of both initial and final dumbbell position) have to be considered, both in the initial and saddle-point configurations, to compute the force-constant matrix and obtain a unique imaginary frequency that corresponds to the unstable vibration mode.

It is interesting to note that the V-Sb exchange barrier is low while the V jump between two equivalent 1NN configurations

is high compared to the bulk V migration: the exchange jump is therefore expected to be highly correlated, which does not lead to long-range solute migration. The vacancy will most likely jump to 2NN, 3NN, or 4NN configurations after a V-Sb exchange sequence. The barrier to dissociate from these configurations is higher than the barrier to come back to 1NN, hence the VSb pair is expected to migrate through back and forth jumps between (1NN) and $(1NN)^2$ shells.

[1] S. J. Zinkle and J. T. Busby, Mater. Today **12**, 12 (2009).
[2] P. Yvon and F. Carré, J. Nucl. Mater. **385**, 217 (2009).
[3] K. C. Russell, J. Nucl. Mater. **83**, 176 (1979).
[4] S. Bruemmer, E. Simonen, P. Scott, P. Andresen, G. Was, and J. Nelson, J. Nucl. Mater. **274**, 299 (1999).
[5] G. Was, *Fundamentals of Radiation Materials Science* (Springer, Berlin, Heidelberg, 2007).
[6] T. R. Anthony, Phys. Rev. B **2**, 264 (1970).
[7] M. Nastar and F. Soisson, Compr. Nucl. Mater., 471 (2012).
[8] A. J. Ardell and P. Bellon, Curr. Opin. Solid State Mater. Sci. **20**, 115 (2016).
[9] A. Barbu and A. Ardell, Scr. Metall. **9**, 1233 (1975).
[10] R. Cauvin and G. Martin, J. Nucl. Mater. **83**, 67 (1979).
[11] G. Martin, Phys. Rev. B **30**, 1424 (1984).
[12] R. Bullough and M. Hayns, J. Nucl. Mater. **57**, 348 (1975).
[13] P. Heald and J. Harbottle, J. Nucl. Mater. **67**, 229 (1977).
[14] J. Matthews and M. Finnis, J. Nucl. Mater. **159**, 257 (1988).
[15] E. Little and D. Stow, J. Nucl. Mater. **87**, 25 (1979).
[16] F. Garner, M. Toloczko, and B. Sencer, J. Nucl. Mater. **276**, 123 (2000).
[17] A. Bhattacharya, E. Meslin, J. Henry, A. Barbu, S. Poissonnet, and B. Décamps, Acta Mater. **108**, 241 (2016).
[18] J. R. Rice and J.-S. Wang, Mater. Sci. Eng.: A **107**, 23 (1989).
[19] M. A. Gibson and C. A. Schuh, Acta Mater. **95**, 145 (2015).
[20] X. Zhang, E. G. Fu, N. Li, A. Misra, Y.-Q. Wang, L. Shao, and H. Wang, J. Eng. Mater. Technol. **134**, 041010 (2012).
[21] L. Liu, Z. Tang, W. Xiao, and Z. Wang, Mater. Lett. **109**, 221 (2013).
[22] W. Han, M. J. Demkowicz, N. A. Mara, E. Fu, S. Sinha, A. D. Rollett, Y. Wang, J. S. Carpenter, I. J. Beyerlein, and A. Misra, Adv. Mater. **25**, 6975 (2013).
[23] A. Vattré, T. Jourdan, H. Ding, M.-C. Marinica, and M. J. Demkowicz, Nat. Commun. **7**, 10424 (2016).
[24] R. A. Enrique and P. Bellon, Phys. Rev. Lett. **84**, 2885 (2000).
[25] X. Zhang, J. Wen, P. Bellon, and R. S. Averback, Acta Mater. **61**, 2004 (2013).
[26] J. Lee, C. R. Lear, X. Zhang, P. Bellon, and R. S. Averback, Metall. Mater. Trans. A **46**, 1046 (2014).
[27] S. Shu, P. Bellon, and R. S. Averback, Phys. Rev. B **91**, 214107 (2015).
[28] J. Leitnaker, E. Bloom, and J. Stiegler, J. Nucl. Mater. **49**, 57 (1973).
[29] J. S. Koehler, J. Appl. Phys. **46**, 2423 (1975).
[30] L. Mansur and M. Yoo, J. Nucl. Mater. **74**, 228 (1978).
[31] L. Mansur, J. Nucl. Mater. **83**, 109 (1979).
[32] T. Kato, H. Takahashi, and M. Izumiya, J. Nucl. Mater. **189**, 167 (1992).
[33] M. Nastar, P. Bellon, G. Martin, and J. Ruste, Mater. Res. Soc. Symp. Proc. **481**, 383 (1998).
[34] J. Gan, E. Simonen, S. Bruemmer, L. Fournier, B. Sencer, and G. Was, J. Nucl. Mater. **325**, 94 (2004).
[35] A. Janotti, M. Krcmar, C. L. Fu, and R. C. Reed, Phys. Rev. Lett. **92**, 085901 (2004).
[36] M. Mantina, Y. Wang, L. Chen, Z. Liu, and C. Wolverton, Acta Mater. **57**, 4102 (2009).
[37] T. Garnier, M. Nastar, P. Bellon, and D. R. Trinkle, Phys. Rev. B **88**, 134201 (2013).
[38] T. Garnier, D. R. Trinkle, M. Nastar, and P. Bellon, Phys. Rev. B **89**, 144202 (2014).
[39] T. Schuler and M. Nastar, Phys. Rev. B **93**, 224101 (2016).
[40] C. P. Flynn, Phys. Rev. **134**, A241 (1964).
[41] R. Cauvin, Ph.D. thesis, Université de Nancy I, 1981.
[42] T. Schuler, Ph.D. thesis, Université Paris Sud XI, 2015.
[43] C. Barouh, T. Schuler, C.-C. Fu, and M. Nastar, Phys. Rev. B **90**, 054112 (2014).
[44] T. Schuler, C. Barouh, M. Nastar, and C.-C. Fu, Phys. Rev. Lett. **115**, 015501 (2015).
[45] C. P. Flynn, Philos. Mag. **10**, 909 (1964).
[46] A. Allnatt and A. Lidiard, *Atomic Transport in Solids* (Cambridge University Press, Cambridge, 2003).
[47] A. Damask and G. Dienes, Acta Metall. **12**, 797 (1964).
[48] R. E. Howard and A. B. Lidiard, Philos. Mag. **11**, 1179 (1965).
[49] M. Nastar, V. Y. Dobretsov, and G. Martin, Philos. Mag. A **80**, 155 (2000).
[50] M. Nastar, Philos. Mag. **85**, 3767 (2005).
[51] T. Garnier, V. R. Manga, D. R. Trinkle, M. Nastar, and P. Bellon, Phys. Rev. B **88**, 134108 (2013).
[52] L. Messina, M. Nastar, T. Garnier, C. Domain, and P. Olsson, Phys. Rev. B **90**, 104203 (2014).
[53] L. Messina, M. Nastar, N. Sandberg, and P. Olsson, Phys. Rev. B **93**, 184302 (2016).
[54] V. Barbe and M. Nastar, Philos. Mag. **87**, 1649 (2007).
[55] V. Barbe and M. Nastar, Phys. Rev. B **76**, 054206 (2007).
[56] A. Lidiard, Philos. Mag. **46**, 1218 (1955).
[57] A. Le Claire, J. Nucl. Mater. **69–70**, 70 (1978).
[58] H. Wu, T. Mayeshiba, and D. Morgan, Sci. Data **3**, 160054 (2016).
[59] A. Le Claire, *Correlation Effects in Diffusion in Solids*, edited by W. Jost (Academic Press, New York and London, 1970), Chap. 5.
[60] H. Mehrer (ed.), in *Diffusion in Solid Metals and Alloys*, Landolt-Börnstein - Group III Condensed Matter Vol. 26 (Springer, Berlin, Heidelberg, 1990).
[61] K. Hoshino, Y. Iijima, and K.-i. Hirano, Trans. Jpn. Inst. Met. **22**, 527 (1981).
[62] B. Predel, Cu-Tl (copper-thallium), in *Cr-Cs – Cu-Zr*, Landolt-Börnstein - Group IV Physical Chemistry Vol. 5D (Springer, Berlin, Heidelberg, 1994).
[63] O. Teppo, J. Niemelä, and P. Taskinen, Thermochim. Acta **185**, 155 (1991).

[64] L. S. Chang, B. B. Straumal, E. Rabkin, W. Gust, and F. Sommer, J. Phase Equilib. **18**, 128 (1997).
[65] B. Predel, Cu-Sb (copper-antimony), in *Cr-Cs – Cu-Zr*, Landolt-Börnstein - Group IV Physical Chemistry Vol. 5D (Springer, Berlin, Heidelberg, 1994).
[66] G. Martin and P. Bellon, Solid State Phys. **50**, 189 (1996).
[67] F. Soisson and T. Jourdan, Acta Mater. **103**, 870 (2016).
[68] H. Ullmaier (ed.), in *Atomic Defects in Metals*, Landolt-Börnstein - Group III Condensed Matter Vol. 25 (Springer, Berlin, Heidelberg, 1991).
[69] A. Glensk, B. Grabowski, T. Hickel, and J. Neugebauer, Phys. Rev. X **4**, 011018 (2014).
[70] E. Clouet, Modeling of nucleation processes, in *ASM Handbook Volume 22a: Fundamentals of Modeling for Metals Processing*, edited by D. U. Furrer and S. L. Semiatin (ASM International Materials Park, Ohio, 2009), pp. 203–219.
[71] T. Jourdan, G. Bencteux, and G. Adjanor, J. Nucl. Mater. **444**, 298 (2014).
[72] A. Badillo, P. Bellon, and R. S. Averback, Modelling Simul. Mater. Sci. Eng. **23**, 035008 (2015).
[73] S. Mao, S. Shu, J. Zhou, R. S. Averback, and S. J. Dillon, Acta Mater. **82**, 328 (2015).
[74] G. Kresse and J. Furthmüller, Phys. Rev. B **54**, 11169 (1996).
[75] J. P. Perdew, K. Burke, and M. Ernzerhof, Phys. Rev. Lett. **77**, 3865 (1996).
[76] P. E. Blöchl, Phys. Rev. B **50**, 17953 (1994).
[77] G. Kresse and D. Joubert, Phys. Rev. B **59**, 1758 (1999).
[78] M. Methfessel and A. T. Paxton, Phys. Rev. B **40**, 3616 (1989).
[79] G. Henkelman, B. P. Uberuaga, and H. Jónsson, J. Chem. Phys. **113**, 9901 (2000).
[80] H. H. Wu and D. R. Trinkle, Phys. Rev. Lett. **107**, 045504 (2011).
[81] R. Agarwal and D. R. Trinkle, Phys. Rev. B **94**, 054106 (2016).
[82] G. H. Vineyard, J. Phys. Chem. Solids **3**, 121 (1957).
[83] C. Kittel, *Introduction to Solid State Physics*, 6th ed. (Wiley, New York, 1986).
[84] G. Simmons and H. Wang, *Single Crystal Elastic Constants and Calculated Aggregate Properties: a Handbook* (MIT Press, Cambridge, MA, 1971).
[85] C. Varvenne, F. Bruneval, M.-C. Marinica, and E. Clouet, Phys. Rev. B **88**, 134102 (2013).
[86] A. R. Akbarzadeh, Z. Z. Chen, and N. Kioussis, Phys. Rev. B **79**, 195404 (2009).
[87] M. Ganchenkova, Y. Yagodzinskyy, V. Borodin, and H. Hänninen, Philos. Mag. **94**, 3522 (2014).